Science and Technology of Welding and Joi

Process parameters selection for multi-layer friction surfacing of 7075 aluminium alloy

Journal:	*Science and Technology of Welding and Joining*
Manuscript ID	STW-24-0054.R2
Manuscript Type:	Original Research Article
Date Submitted by the Author:	09-Jul-2024
Complete List of Authors:	Li, Jishuai; Université catholique de Louvain Jadot, Matthieu; Université catholique de Louvain Xie, Jichang; Université de Technologie de Compiègne Lezaack, Matthieu; Université catholique de Louvain Sapanathan, Thaneshan; Curtin University Gautier, Romain; UCLouvain Rachik, Mohamed; Université de Technologie de Compiègne Simar, Aude; Université catholique de Louvain, iMMC
Keywords:	Solid-state additive manufacturing, Friction surfacing, Aluminum alloy, Grain size, Strengthening precipitates, Mechanical properties
Abstract:	The effect of deposition parameters on the microstructure and mechanical properties are studied in multi-layer friction surfacing of 7075 aluminium alloy. These multi-layer structures were successfully manufactured after a parametric study which allows the generation of a deposition window, including an interface quality comparison. A higher rotational speed leads to a larger grain sizes. The coarse precipitates size and volume fraction decrease along the build direction in correlation with the thermal cycles profile. The top layer has a higher hardness after deposition, while bottom layers are in annealed state due to the growth of the strengthening phases. Fracture surface analysis revealed that transversal cracks are due to interlayer decohesion and that voids nucleated on the coarse precipitates.

Process parameters selection for multi-layer friction surfacing of 7075 aluminium alloy

Jishuai Li [1,2*], Matthieu Jadot [1,3], Jichang Xie [4], Matthieu B. Lezaack [1], Thaneshan Sapanathan[1,5], Romain Gautier [1,3], Mohamed Rachik [4], Aude Simar [1,3]

[1] Institute of Mechanics, Materials and Civil Engineering, Université Catholique de Louvain, 1348, Louvain-la-Neuve, Belgium

[2] CRRC Technology Innovation (Beijing) Co., Ltd, Beijjing, China

[3] WEL Research Institute, 1300 Wavre, Belgique

[4] Laboratoire Roberval, UTC, Sorbonne Universités, Université de Technologie de Compiègne, Centre de recherche Royallieu, CS60319, 60203 Compiègne Cedex, France

[5] Curtin Corrosion Centre, WA School of Mines: Minerals, Energy and Chemical Engineering, Faculty of Science and Engineering, Curtin University, Perth, WA, Australia

*Corresponding author: jishuai.li@outlook.com

Abstract:

The effect of deposition parameters on the microstructure and mechanical properties are studied in multi-layer friction surfacing of 7075 aluminium alloy. These multi-layer structures were successfully manufactured after a parametric study which allows the generation of a deposition window, including an interface quality comparison. A higher rotational speed leads to a larger grain sizes. The coarse precipitates size and volume fraction decrease along the build direction in correlation with the thermal cycles profile. The top layer has a higher hardness after deposition, while bottom layers are in annealed state due to the growth of the strengthening phases. Fracture surface analysis revealed that transversal cracks are due to interlayer decohesion and that voids nucleated on the coarse precipitates.

Keywords: Solid-state additive manufacturing; Friction surfacing; Aluminum alloy; Grain size; Strengthening precipitates; Mechanical properties

1. Introduction

Fusion based additive manufacturing (AM) of "non-weldable" high performance 7xxx series aluminium alloys remain a challenging task. Multi-layer friction surfacing (MLFS) and additive friction stir deposition (AFSD) were developed in recent years as novel solid-state AM technologies. These processes leverage the fundamental physics of friction stir welding and processing (FSW/P) [1]. Among the variety of solid-state AM technologies, MLFS and AFSD show competitive advantages as their ability to use solid feedstock [2], metallic powder [3,4] or recycled machine chips [5,6] to additively build parts or as a mean of repairing parts.

Compared to AFSD using specifically designed AM machines, MLFS can easily be performed by any FSW machine or on a computer numerical control (CNC) machine. This would promote the widespread use of MLFS in engineering applications. MLFS creates deposited layers by pressing a rotating consumable solid feedstock against a substrate or previous layers. A strong metallurgical bond is achieved through frictional heat and severe plastic deformation. However, MLFS is more prone to weak interfacial bonding and residual porosity between layers due to the lack of deposition control. Therefore, the first aim of our work will be to carry out a parametric study to build strong interfaces using MLFS process.

The deposition performances depend on the MLFS process parameters and mainly on axial force (F), rotational speed (ω) and traverse speed (ν) (Fig. 1a). Several studies have optimized MLFS based on friction surfacing (FS), i.e., for a monolayer [1,8]. The deposition efficiency is evaluated by the fraction of the feedstock actually deposited. It is thus correlated with the FS deposition geometry [9]. It is generally found that the deposition width increases with decreasing ω and ν at low F [10], and the deposit became thinner when the feedstock is applied with increasing ω, ν or F [11]. The bonding strength decreases with a larger transverse speed (ν), which is an interesting parameter to favour deposition productivity. The vertical force F is the dominant parameter favouring a fully bonded interface [12]. However, width, thickness and bonding of the interface are material dependant, for fixed processing conditions and parameters [9]. Indeed, it was demonstrated that increasing the Mg content of AA6060 leads to the prominence of shear flow localization, resulting in thinner and narrower depositions [13].

Currently, there is a lack of available results on the effect of FS deposition parameters for the classical and high strength AA7075 and their effect on microstructural heterogeneities, which lead to another challenge in this work: the development of MLFS for AA7075.

In 7xxx Al series, η' and η precipitates are present in peak-aged T6 state. These hardening precipitates are typically composed of $MgZn_2$, in a semi-coherent state for planar η' precipitates and non-coherent state for the thicker η precipitates [14]. However, coarser η nucleate and grow by preferential precipitation at grain boundaries [15]. In friction stirred structures made of 7xxx Al alloys, as-processed microstructure typically consists in a refined stir zone, showing over-aged coarser η precipitates at the grain boundaries, while some solid solution of alloying element is also evidenced in this stir zone [16,17]. The microstructural features encountered in FSW/P of 7xxx alloys should be observable in the FS and MLFS of AA7075.

The microstructure is influenced by thermal cycles during MLFS and a refinement of the grain size is observed due to dynamic recrystallization [18]. Few studies have investigated the microstructure and mechanical properties of FS monolayers [9,18]. Whereas the repetitive thermal cycles involve microstructural changes due to the addition of the layers that MLFS implied. Strengthening precipitates over-aging was observed in MLFS of AA2014 without further analysis about the evolution of precipitates along the deposition height [19]. Rath *et al.* studied the influence of successive deposition cycles on the interface layer and anisotropy of MLFS AA5083 [20]. They reported no significant gradient in hardness along the length and height of the deposit, as expected in non-age hardenable 5xxx series. In contrast, layered nature and complex thermal history of MLFS are believed to influence the microstructure and mechanical properties of precipitate hardened aluminium alloys (7xxx series), e.g., by dissolution and coarsening of η’ and η hardening precipitates in AA7075.

The aim of the present study is to develop the understanding of MLFS characteristics for a heat treatable aluminium alloy of the 7xxx series, highly influenced by multiple thermal cycles.

2. Experimental methods

2.1 Materials and processing

The deposition tests were performed on a dedicated FSW machine (FSW-LM-AM-16-2D, Tra-C industries). A 3D schematic illustration of the MLFS process is shown in Fig.1a. The substrate material is an AA6061 in T6 state. The initial feedstock is an AA7075 rod in T6 state, having a diameter of 20 mm and length of 120 mm. These rods are used as consumables for FS and MLFS. Prior to depositing the AA7075 multi-layer structures, a parametric study for single layers was carried out. The FS depositions were performed with the force ranging from 5 to 15 kN, ω varying from 300 to 1200 rpm, and ν ranging from 60 to 280 mm/min.

Based on that, two processing parameter sets are selected (Section 3.2) and studied for MLFS process: Deposition Specimen 1 (DS1) is 5 kN, 180 mm/min, 1000 rpm and Deposition Specimen 2 (DS2) is 5 kN, 180 mm/min, 800 rpm. For both DS1 and DS2, the whole deposition process is controlled by a constant axial force command of the machine. The interval between deposition layers is around 12 minutes, this allows enough time for changing the consumable rod and allows the deposition to reach room temperature. Selected investigation zones used for the analysis, located at mid-height of various layers, are given in Fig 1e.

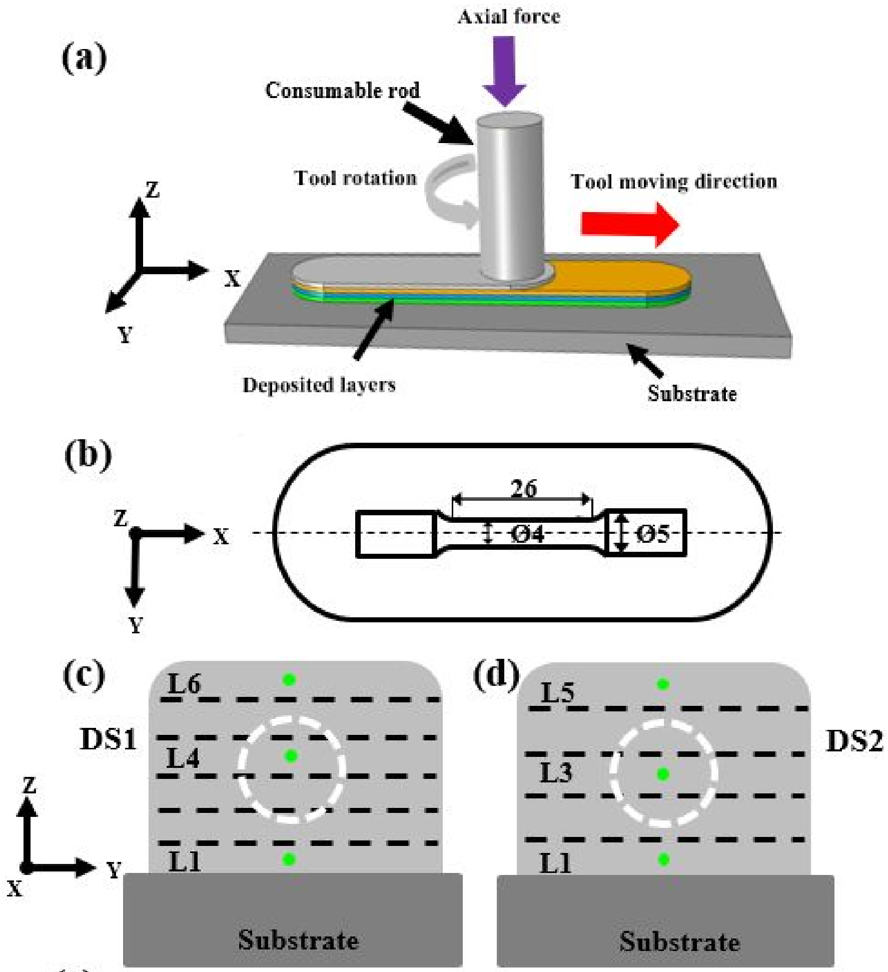

(e)

DS1	Top of the substrate	1	4	6	**Layer (n°)**
	0	0.9	5.6	8.7	**Z position (mm)**
DS2	Top of the substrate	1	3	5	**Layer (n°)**
	0	0.9	4.7	8.1	**Z position (mm)**

Fig. 1. (a) 3D schematic illustration of the MLFS process. (b) Geometry and extraction position of tensile samples, with X-axis as loading direction. (c-d) Schematic illustration of the middle positions in the selected layers (green points) and the tensile samples positions (white circles) in the two selected specimens, DS1 and DS2. (e) Investigated zone positions (green points in c and d) for DS1 (1000 rpm) and DS2 (800 rpm).

2.2 Microstructure characterization

The samples used for FS characterization were cut parallel to the Y-Z plane (Figs. 1a-d). Then, following the standard metallurgical sample preparation procedures, they were characterized by optical microscopy with a Keyence VHX-7000 microscope and by Scanning

Electron Microscopy (SEM) on a FEGSEM ULTRA 55 microscope. Electron Backscatter diffraction (EBSD) imaging is performed with a field emission gun SEM (Zeiss ΣigmaTM), under the conditions of an accelerating voltage of 10 kV, a tilt of 70°, a working distance of 20 mm, and a step of 100 nm and 70 nm based on the grain size. EBSD maps were post-processed with Oxford AZtecCrystal software. A Transmission Electron Microscopy (TEM) lamella is extracted in the middle of L1 of DS2 and observed by a CM20 Philips under 200 kV.

Coarse precipitates analysis and the EBSD observations are consistent with the positions shown in Figs.1c-d, i.e., the bottom layer (L1), the top layer (L6 for DS1 and L5 for DS2) and an intermediate layer (L4 for DS1 and L3 for DS2).

2.3 Mechanical testing

EMCO-TEST DuraScan G5 tester was used to measure microhardness of the depositions and initial feedstock. A 0.1 kg load and 0.5 mm indent spacing were selected in this study.

Uniaxial tensile tests of the MLFS were performed on smooth cylindrical dog-bone shaped samples with a diameter of 4 mm and a gauge length of 26 mm (Figs. 1b-d) using a Zwick Tensile machine. For the initial feedstock, the tensile specimens were extracted along the extrusion direction. The strain was measured using a gauge length extensometer. The crosshead speed was 1 mm/min during the test. Fracture surfaces were characterized using SEM to evidence the fracture mechanisms of the MLFS depositions.

3. Results and discussion

3.1 Effects of processing parameters on depositions

Various combinations of process parameters were investigated to build monolayers of the AA7075. Some conditions leading to the absence of adherence between the substrate and the deposition were directly discarded, i.e., for the parameters F = 5 kN, v = 120 mm/min, and ω =

300 rpm (Fig.2a). When ν is decreased to 100 mm/min and ω is increased to 800 rpm, the deposition adheres to the substrate (Fig.2b).

The cross-section of the monolayers with successful deposition were further investigated to evaluate their quality. The successful depositions are highlighted in Fig.3a-b. Figs.2c-e reveal two typical interface morphologies, including:

- The defected interface type which was not selected because it exhibited a significant amount of voids all along the interface (Fig.2c).
- The non-defected interface type, the desired case, a good bonding was found between the deposition and the substrate (Fig.2d-e). This deposition displays either an interface with the substrate without voids in the middle zone (Fig.2d) or a highly mixed interface (Fig.2e). This implies a strong bond between the layer and the substrate.

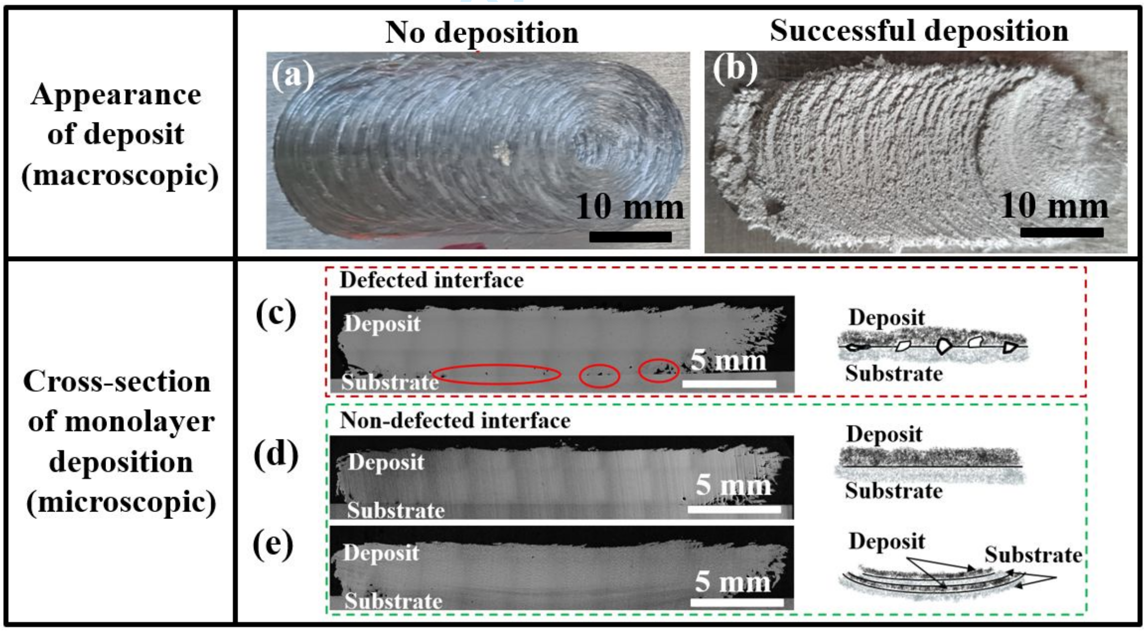

Fig. 2. (a-b) Photographs showing the overall appearance of the FS specimens. No deposition is achieved (a), successful deposition (b). (c-e) Three cross-sections of monolayer depositions divided into two interface type for the parameters of Figs.3a-b, i.e., with voids for the defected interface type (c), with non-defected interface type without voids (d) and, with a highly mixed interface (e).

3.2 Deposition window and selection of two processing parameters

Fig.3a shows the deposition window obtained by varying F and v while keeping ω constant at 800 rpm. Successful depositions cannot be achieved with F lower than 5kN and v higher than 200 mm/min due to insufficient deformation and/or heat generated. Fig.3b presents the deposition window obtained by varying ω and v with a constant axial force F of 5 kN, that was selected as the minimum required vertical force for sound deposition. Now, ω lower than 800 rpm and a v higher than 200 mm/min do not lead to any deposition. Thus, appropriate values are $F \geq 5$kN, $v \leq 200$ mm/min and $\omega \geq$ 800 rpm.

In this study, the two selected sets of parameters, DS1 (5 kN, 180 mm/min, 1000 rpm) and DS2 (5 kN, 180 mm/min, 800 rpm), exhibited a clearly "non-defected interface type" and are used to investigate the microstructure and mechanical evolution during MLFS (see Figs.3a-b). Figs.3c-d show the cross-sectional micrographs of the specimens exhibiting metallurgically bonded layers in the centre of the interface. One should note that porosity and unbounded interface are visible at the edges on the advancing side and retreating side. Those defects are inherent to the absence of non-consumable shoulder during MLFS compared to the AFSD process (section 1). Note that DS1 and DS2 consist of 6 and 5 layers respectively with similar final deposition height.

Fig.3e provides the geometry of each layer (see also supplementary data). It indicates that decreasing ω from 1000 rpm (DS1) to 800 rpm (DS2) slightly increases the deposited layer thickness, showing the relation between the rotational speed and the thickness. This phenomenon is also confirmed by the parametric study of the monolayer deposition profile which was investigated based on the transverse speed, rotational speed, and axial force.

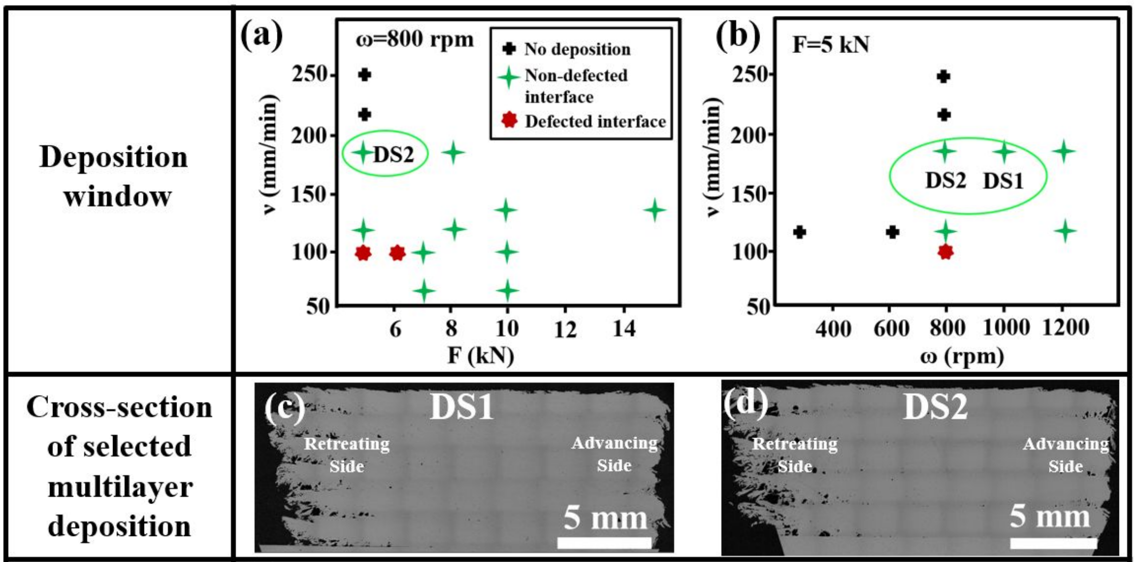

Overview of the deposition geometry

(e)

Sample	Average thickness of one layer with its variance (mm)	Average width of one layer with its variance (mm)	Length of the layers (mm)
DS1	1.65 ± 0.04	22.74 ± 1.02	270
DS2	1.76 ± 0.15	22.92 ± 1.77	360

Fig. 3. (a) Deposition window varying on F and v with ω = 800 rpm for the corresponding interface types (Figs.2c-e). (b) Deposition window varying on ω and v with F = 5 kN for the corresponding interface types (Figs.2c-e). (c-d) Cross-sectional micrography of the selected DS1 (1000 rpm) - DS2 (800 rpm), respectively. (e) Table of the deposition geometry of each layer (average thickness, width with the relative variance and length).

3.3 Grain structure and size distribution

Fig.4a shows the EBSD inverse pole figure maps taken from the middle area of the selected layers in DS1 and DS2 (Fig.1c-d). EBSD images show refined equiaxed grains in all areas due to dynamic recrystallization (DRX). Indeed, the material is subjected to large plastic deformation due to the shearing of the fresh overlaying material between the feed rod and the previous layer/substrate, leading to DRX. Note that it is expected that static recrystallization and subsequent grain growth also occurs during the cooling stage.

Fig.4b presents the average grain size with standard deviation as a function of different rpm and positions in the MLFS structure. The feedstock exhibits a grain size of 3.3µm ± 4.6µm with a bimodal size distribution including small grains up to 0.4µm and larger grains up to 40.4 µm. The feedstock grain size is reduced by 57% and 65% for samples DS1 and DS2, respectively. DS1 specimen exhibits larger grains than DS2 at equivalent position in the MLFS structure, with an average grain size of 1.4 μm ± 0.7μm and 1.2 μm ± 0.6μm, respectively. The increasing grain size from DS1 to DS2 is related to the increase in heat input due to a rotational speed increases, as demonstrated by Kallien *et al.* [21]. This indicates that DRXed grain size can be controlled by altering the amount of heat generated via parameter-controlled friction surfacing process.

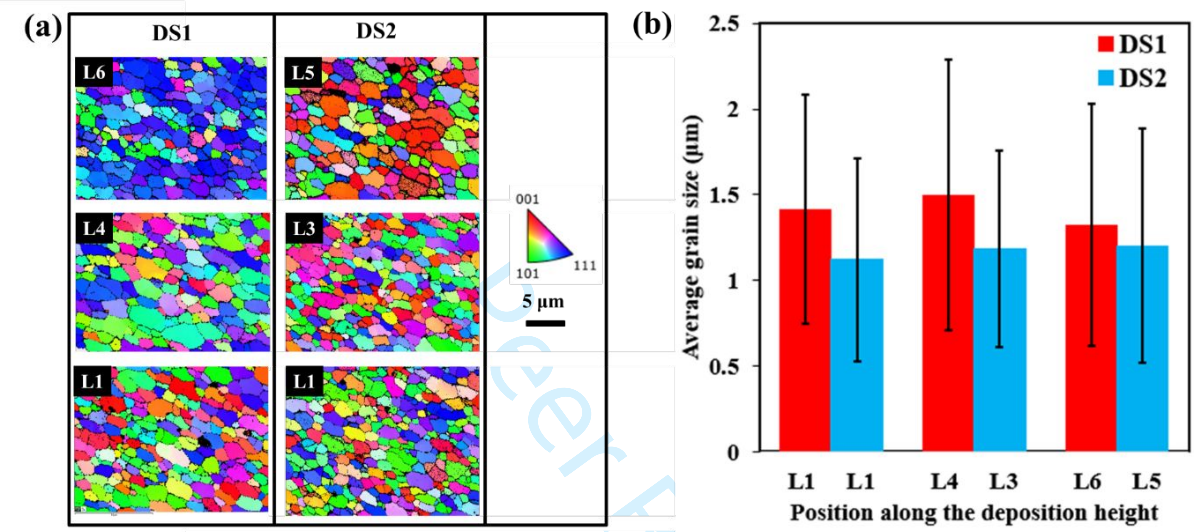

Fig. 4. (a) EBSD inverse pole figure maps in the different positions (Figs.1c-d) of DS1 and DS2, respectively. (b) Average grain size of DS1 and DS2.

3.4 Coarse precipitates evolution

Fig.5a presents the SEM images of grain boundary precipitates for DS1 and DS2 in the middle area of the selected layers (Figs.1c-d). A collection of precipitates (e.g., red arrows in Fig.5a) are clearly visible along the grain boundaries. These precipitates, including η-precipitates, are confirmed by the TEM image and related diffraction pattern, Fig.5b. Considering the non-statistical character of TEM observations, coarse precipitates are quantified on SEM images using image analysis. Fig.5c shows that the mean precipitate size is decreasing from the bottom to the top layer for both specimens ranging from 100 nm to 150 nm. Fig.5d also shows a decrease of the coarse precipitates surface fraction.

The higher precipitate volume fraction/size in the bottom layer (L1) is induced by repetitive heating cycles required for building upper layers. The lower the layer, the more thermal cycles it undergoes. Contrarily to the grain size, accumulated heat directly explains the observed trends in precipitates populations. No evident difference between DS1 and DS2 samples can be identified except for the top layer (higher precipitate size and lower precipitate density for DS1).

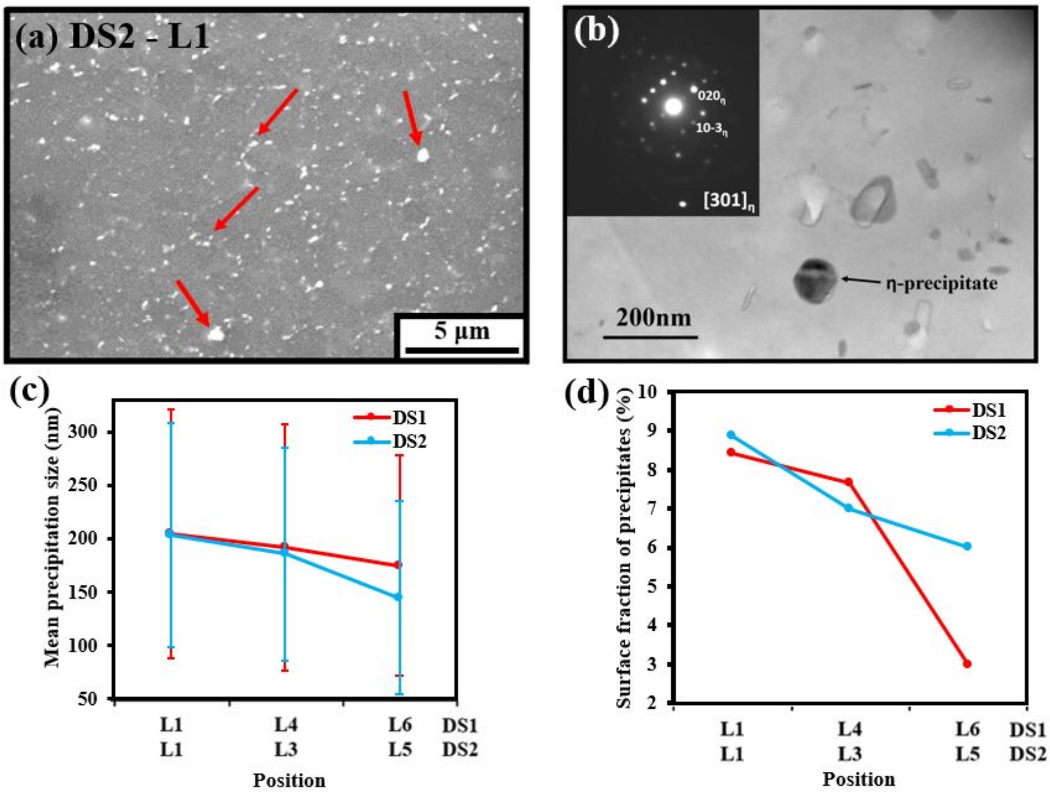

Fig. 5. (a) SEM image of the precipitates distribution in the layer 1 middle area for DS2. It shows coarse precipitates (red arrows). (b) TEM image shows the coarse precipitates and identification of an η precipitate (diffraction pattern) (c) Coarse precipitates mean size based on SEM images. (d) Surface fraction of coarse precipitates based on SEM images.

3.5 Mechanical properties

3.5.1 Microhardness evolution

Fig.6 shows the average microhardness of DS1 and DS2 along the thickness direction of the specimens. The depositions are softer (95 to 130HV) than the initial T6 feedstock

(171±4HV). Moreover, both samples exhibit a similar hardness gradient along the Z position, i.e., increase gradually from bottom to top layers. Such a hardness gradient along the deposition height was not reported in previous studies performed on MLFS AA5083 [22] because it is not a heat treatable alloy, while AA7075 is heat-sensitive in terms of precipitation. MLFS leads to a non-homogeneous hardening precipitation throughout the built structures.

Indeed, the fraction of coarse precipitates decrease in the built direction (Fig.5) but these precipitates are not contributing to the strengthening due to their size. Hardening precipitates are in the range of 5 nm to 10 nm in peak-aged state for 7075 alloy. Thus, observed coarse precipitates of Fig.5 are absorbing the alloying elements in non-hardening coarse precipitates. Therefore, the lower the coarse density, the higher the amount of alloying elements for fine strengthening precipitates (or solid solution atoms). One should indeed notice that the hardness follows the opposite trend to the density of coarse precipitates.

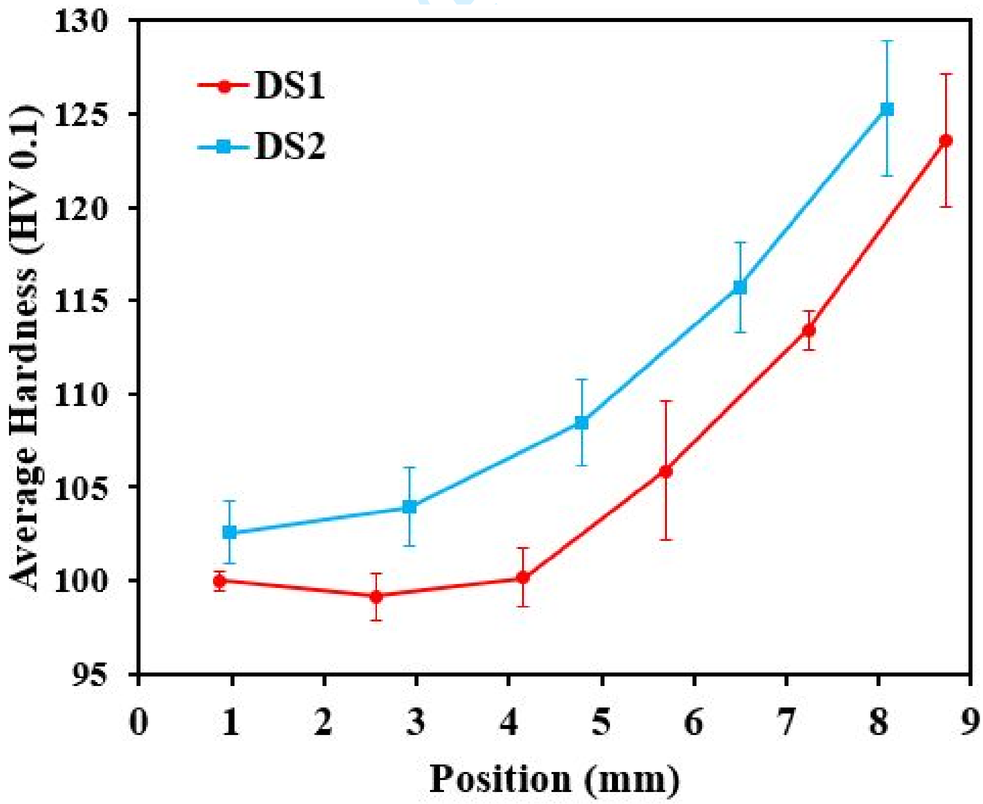

Fig. 6. Average hardness in Z position for both samples, DS1 (1000 rpm) and DS2 (800 rpm). Note that the scale only spans over 30 HV to highlight the small difference between DS1 and DS2.

Interestingly, the average hardness of DS2 (800 rpm, cooler condition) is slightly higher than that of DS1 (1000 rpm) regardless of the layer position, despite sometimes a higher coarse precipitates density (i.e. in the top layer). This breaks the inverse trend mentioned just above. DS1 presents an additional layer compared to DS2 and thus experiences one more thermal cycle for a similar final height compared to DS2 (DS1 has 6 layers and DS1 has 5 layers). This additional thermal cycle can overage further the material and results in potential overgrowth of the efficient η'- η precipitates that remain after the deposition. It is expected that lower heat input lead to harder microstructure in FSW/P of age hardenable alloys, confirming the relationship between friction-stir base processes and FS/MLFS. Moreover, this small difference can come from a grain size effect. Indeed, by Hall-Petch law, the smaller grains the higher the yield strength and consequently the hardness. This is following the difference of the DS1 and DS2 grain size with the Hall-Petch law:

$$\Delta\sigma_d = \frac{\mathrm{k_d}}{\sqrt{\mathrm{d_{DS2}}}} - \frac{\mathrm{k_d}}{\sqrt{\mathrm{d_{DS1}}}} = 3.3\ [MPa]$$

where σ_d is the strength associated to the grain size, k_d is a constant ~0.04 MPa $m^{-1/2}$ in aluminium, and d_{DS} is the grain size [23]. The hardness is roughly estimated as one third of the yield strength [24], meaning a ΔH_v of 1.1 HV. Although, this seems to correspond to the difference in Fig. 6, it is a rather negligible difference as 1.1 HV is below 1.1 % of the total microhardness.

3.5.2 Tensile behaviour

Fig.7 shows a comparison between the true stress-strain curves of initial feedstock, DS1, and DS2. The initial feedstock material exhibited the highest yield strength of 578 MPa with an ultimate tensile strength of 634 MPa. The strength reduction of the MLFS structures is due to the overgrowth of the strengthening phases (Section 3.4). DS2 presents a slightly higher final true stress due to a higher ductility compared to DS1. The strengths and stresses of the specimens are not significantly different correlating the hardness observations (Fig. 6).

Moreover, Fig.7 shows a few bumps in the stress–strain curves (inset in Fig. 7). This effect could be due to interlayer decohesion or possibly to Portevin-Le Chatelier (PLC) effect, i.e. solute atoms causing dynamic strain aging [25, 26].

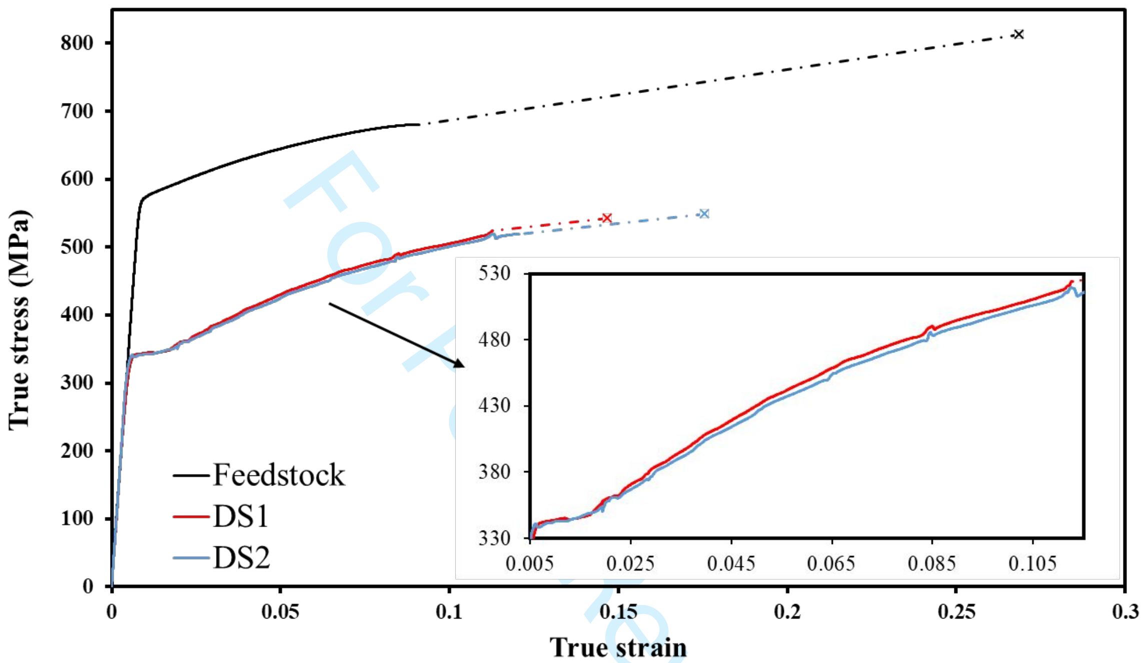

Fig. 7. True stress-strain curves for the feedstock, DS1, and DS2.

Fig.8 displays SEM images of representative fracture surfaces of the tensile samples of Fig.7. The macroscopic fracture surfaces, Figs.8a-b, show that the crack propagation paths are influenced by the multi-layer microstructure with interlayer decohesion cracks. These cracks are in a plane parallel to the loading direction (see also Figs.8a1-b1). This interlayer decohesion is facilitated by interfacial defects that remains from manufacturing and act as crack initiation sites (Fig.3c-d), particularly at the edges of the specimen. Early crack propagation thus occurs in the interlayer zone, while the deposited layers act as more resistant ligaments of material.

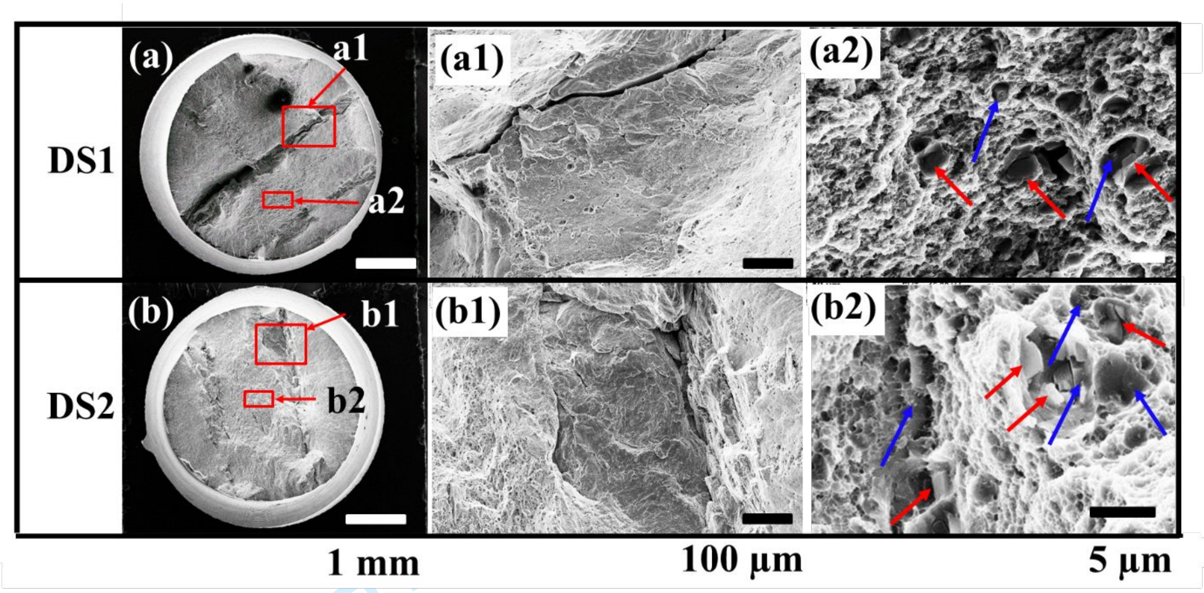

Fig. 8. SEM micrographs showing fracture surfaces from tensile samples. (a) and (b) Low magnification of DS1 and DS2, respectively. (a1), (b1), (a2) and (b2) Higher magnification images of the areas marked in (a) and (b), respectively. The intermetallic particles (red arrows) and coarse precipitates (blue arrows) are highlighted.

In addition, the fracture surface within one layer is characterized by dimples presenting different sizes. Coarse Fe-rich intermetallic particles are clearly evidenced inside the larger dimples for all tensile samples (red arrows in Figs.8a2 and b2). Smaller dimples surround the coarser ones and expectedly nucleated on coarse precipitates (blue arrows in Figs.8a2 and b2). They indicate that the tensile specimens exhibit intra-layer ductile fracture characterised by void nucleation and growth of primary void population on broken intermetallic particles followed by a secondary void nucleation on coarse precipitates prior to failure [27, 28].

The fracture mechanism for MLFS specimens is thus influenced by its intrinsic microstructure, with a competition between decohesion of the interface and the ductile tearing of the deposition layers followed by the ductile failure of the remaining material ligaments. This can be related to the rolled 7xxx Al alloys failure mechanisms, where large elongated grained structures fail by a competition of grains delamination and grain interior ductile fracture [15].

4. Conclusions

Experimental analysis investigates the effects of the process parameters on Friction Surfacing (FS) of AA7075 deposition. Based on the deposition window, two Multi-Layer Friction Surfacing (MLFS) specimens were successfully manufactured. The influence of the rotational speed on microstructure, hardness and tensile properties was investigated. The following conclusions are summarized:

(1) AA7075 deposition layers made by FS were evaluated in a parametric study. A process window was identified in terms of deposition speed (slower than 200 mm/min), rotational speed (higher than 800 rpm), and deposition force (higher than 5kN). The interface mixing between the layer and the substrate was analysed for each deposition condition, allowing a selection of two promising MLFS parameters.

(2) The MLFS specimens are characterized by the same axial force (5 kN) and traverse speed (180 mm/min) but distinguished by their rotational speeds: 1000 rpm for DS1 and 800 rpm for DS2. Cross-sections of both specimens reveal low defects in the centre, while edges remain porous.

(3) The grain size of the samples is reduced compared to the feedstock alloy. Dynamic recrystallization occurs during deposition combined with static recrystallization and grain growth during the post-deposition cooling stage. The grain size of the higher rotational speed DS1 is larger than that of DS2, in the dense central areas of the layers. The coarse precipitates size/volume fraction decrease from the bottom to the top layer for both cases, as multiple thermal cycles induce further coarsening of the precipitates in bottom layers.

(4) Both depositions show a microhardness reduction compared to initial feedstock due to the overgrowth of the precipitates that absorb most of the alloying elements. The fine hardening precipitation (η' and fine η) is thus annealed by the multiple heating cycles in bottom layers and turned into large precipitates. Cooler condition (800 rpm) gives slightly higher hardness than warmer condition (1000 rpm) at the same deposition height.

(5) Mechanical properties of the deposition are lower than those of T6 base feedstock. Post-fracture analysis reveals that specimens failed at lower ductility than the feedstock due to a competition between layers decohesion and ductile failure of the inner layers. Impurities and larger precipitates act as damage nucleation sites.

This work proves that manufacturing 3-D structuring by solid-state MLFS of AA7075 is feasible. Despite the multiple heat cycles, intermediate strength structures with significant ductile behaviour were produced. Further improvement of the interface quality could pave the way for future ductility improvements.

Acknowledgements

J.L. and A.S. acknowledges the European Research Council [Starting grant - 716678] during his postdoc at UCLouvain. A.S., M.J. and R.G. acknowledge the Walloon Excellence in Technology (WEL-T) research institute [Advanced grant - WEL-T-CR-2023 A – 10]. The authors would like to thank the members of the LACaMI platform for providing equipment and expertise at UCLouvain.

Reference

[1] J. Gandra, H. Krohn, R.M. Miranda, P. Vilaça, L. Quintino, J.F. Dos Santos, Friction surfacing—A review, J Mater Process Technol 214 (2014) 1062–1093. https://doi.org/10.1016/J.JMATPROTEC.2013.12.008.

[2] E. Seidi, S.F. Miller, Feasibility of multilayer solid-state deposition via lateral friction surfacing for metal additive manufacturing, Journal of Materials Research and Technology 20 (2022) 1708–1725. https://doi.org/10.1016/J.JMRT.2022.07.158.

[3] B. Chaudhary, N.K. Jain, J. Murugesan, V. Patel, Exploring temperature-controlled friction stir powder additive manufacturing process for multi-layer deposition of aluminum alloys, Journal of Materials Research and Technology 20 (2022) 260–268. https://doi.org/10.1016/J.JMRT.2022.07.049.

[4] A. Mukhopadhyay, P. Saha, Mechanical and microstructural characterization of aluminium powder deposit made by friction stir based additive manufacturing, J Mater Process Technol 281 (2020) 116648. https://doi.org/10.1016/J.JMATPROTEC.2020.116648.

[5] J.K. Yoder, G.D. Hahn, N. Zhao, R.E. Brennan, K. Cho, H.Z. Yu, Additive friction stir deposition-enabled upcycling of automotive cast aluminum chips, Additive Manufacturing Letters 4 (2023) 100108. https://doi.org/10.1016/J.ADDLET.2022.100108.

[6] J.B. Jordon, P.G. Allison, B.J. Phillips, D.Z. Avery, R.P. Kinser, L.N. Brewer, C. Cox, K. Doherty, Direct recycling of machine chips through a novel solid-state additive manufacturing process, Mater Des 193 (2020) 108850. https://doi.org/10.1016/J.MATDES.2020.108850.

[7] D.Z. Avery, B.J. Phillips, C.J.T. Mason, M. Palermo, M.B. Williams, C. Cleek, O.L. Rodriguez, P.G. Allison, J.B. Jordon, Influence of Grain Refinement and Microstructure on Fatigue Behavior for Solid-State Additively Manufactured Al-Zn-Mg-Cu Alloy, Metall Mater Trans A Phys Metall Mater Sci 51 (2020) 2778–2795. https://doi.org/10.1007/s11661-020-05746-9.

[8] M.E. Özcan, The influence of parameters on the evolution of the friction surfacing method - a review, Journal of Mechanical Science and Technology 36 (2022) 723–730. https://doi.org/10.1007/s12206-022-0120-z.

[9] S. Hanke, J.F. dos Santos, Comparative study of severe plastic deformation at elevated temperatures of two aluminium alloys during friction surfacing, J Mater Process Technol 247 (2017) 257–267. https://doi.org/10.1016/j.jmatprotec.2017.04.021.

[10] H. Sakihama, H. Tokisue, K. Katoh, Mechanical Properties of Friction Surfaced 5052 Aluminum Alloy * 1, n.d.

[11] Z. Kallien, L. Rath, A. Roos, B. Klusemann, Experimentally established correlation of friction surfacing process temperature and deposit geometry, Surf Coat Technol 397 (2020). https://doi.org/10.1016/j.surfcoat.2020.126040.

[12] J. Gandra, D. Pereira, R.M. Miranda, P. Vilaça, Influence of process parameters in the friction surfacing of AA 6082-T6 over AA 2024-T3, in: Procedia CIRP, Elsevier B.V., 2013: pp. 341–346. https://doi.org/10.1016/j.procir.2013.05.058.

[13] J. Ehrich, A. Roos, B. Klusemann, S. Hanke, Influence of Mg content in Al alloys on processing characteristics and dynamically recrystallized microstructure of friction surfacing deposits, Materials Science and Engineering A 819 (2021). https://doi.org/10.1016/j.msea.2021.141407.

[14] P.A. Rometsch, Y. Zhang, S. Knight, Heat treatment of 7xxx series aluminium alloys - Some recent developments, Transactions of Nonferrous Metals Society of China (English Edition) 24 (2014) 2003–2017. https://doi.org/10.1016/S1003-6326(14)63306-9.

[15] M.B. Lezaack, F. Hannard, L. Zhao, A. Orekhov, J. Adrien, A. Miettinen, H. Idrissi, A. Simar, Towards ductilization of high strength 7XXX aluminium alloys via microstructural modifications obtained by friction stir processing and heat treatments, Materialia (Oxf) 20 (2021) 101248. https://doi.org/10.1016/J.MTLA.2021.101248.

[16] D. Jacquin, G. Guillemot, A review of microstructural changes occurring during FSW in aluminium alloys and their modelling, J Mater Process Technol 288 (2021). https://doi.org/10.1016/j.jmatprotec.2020.116706.

[17] D. Yadav, R. Bauri, N. Chawake, Fabrication of Al-Zn solid solution via friction stir processing, Mater Charact 136 (2018) 221–228. https://doi.org/10.1016/j.matchar.2017.12.022.

[18] U. Suhuddin, S. Mironov, H. Krohn, M. Beyer, J.F. Dos Santos, Microstructural evolution during friction surfacing of dissimilar aluminum alloys, Metall Mater Trans A Phys Metall Mater Sci 43 (2012) 5224–5231. https://doi.org/10.1007/s11661-012-1345-8.

[19] J.J.S. Dilip, G.D. Janaki Ram, Microstructure evolution in aluminum alloy AA 2014 during multi-layer friction deposition, Mater Charact 86 (2013) 146–151. https://doi.org/10.1016/J.MATCHAR.2013.10.009.

[20] L. Rath, Z. Kallien, A. Roos, J.F. dos Santos, B. Klusemann, Anisotropy and mechanical properties of dissimilar Al additive manufactured structures generated by multi-layer friction surfacing, International Journal of Advanced Manufacturing Technology (2023). https://doi.org/10.1007/s00170-022-10685-3.

[21] Z. Kallien, B. Klusemann, Combined experimental-numerical analysis of the temperature evolution and distribution during friction surfacing, Surf Coat Technol 437 (2022). https://doi.org/10.1016/j.surfcoat.2022.128350.

[22] J. Shen, S. Hanke, A. Roos, J.F.D. Santos, B. Klusemann, Fundamental study on additive manufacturing of aluminum alloys by friction surfacing layer deposition, in: AIP Conf Proc, American Institute of Physics Inc., 2019. https://doi.org/10.1063/1.5112691.

[23] A. Simar, Y. Bréchet, B. De Meester, A. Denquin, T. Pardoen, Sequential modeling of local precipitation, strength and strain hardening in friction stir welds of an aluminum alloy 6005A-T6, Acta Materialia, 55 (2007) 6133-6143. https://doi.org/10.1016/j.actamat.2007.07.012.

[24] P. Zhang, S. X. Li, Z. F. Zhang, General relationship between strength and hardness, Materials Science and Engineering: A, 529 (2011) 62-73. https://doi.org/10.1016/j.msea.2011.08.061.

[25] P. Zhang, K. Shi, J. Bian, J. Zhang, Y. Peng, G. Liu, A. Deschamps, J. Sun, Solute cluster evolution during deformation and high strain hardening capability in naturally aged Al–Zn–Mg alloy, Acta Mater 207 (2021) 116682. https://doi.org/10.1016/J.ACTAMAT.2021.116682.

[26] D. Wu, W. Li, X. Liu, Y. Gao, Q. Wen, A. Vairis, Effect of material configuration and welding parameter on weld formability and mechanical properties of bobbin tool friction stir welded Al-Cu and Al-Mg aluminum alloys, Mater Charact 182 (2021) 111518. https://doi.org/10.1016/J.MATCHAR.2021.111518.

[27] T. Ueda, L. Helfen, T.F. Morgeneyer, In situ laminography study of three-dimensional individual void shape evolution at crack initiation and comparison with Gurson-Tvergaard-Needleman- type simulations, Acta Mater 78 (2014) 254–270. https://doi.org/10.1016/j.actamat.2014.06.029.

[28] D. Fabrègue, T. Pardoen, A constitutive model for elastoplastic solids containing primary and secondary voids, J Mech Phys Solids 56 (2008) 719–741. https://doi.org/10.1016/j.jmps.2007.07.008

Process parameters selection for multi-layer friction surfacing of 7075 aluminium alloy

Jishuai Li [1,2*], Matthieu Jadot [1,3], Jichang Xie [4], Matthieu B. Lezaack [1], Thaneshan Sapanathan[1,5], Romain Gautier [1,3], Mohamed Rachik [4], Aude Simar [1,3]

[1] Institute of Mechanics, Materials and Civil Engineering, Université Catholique de Louvain, 1348, Louvain-la-Neuve, Belgium

[2] CRRC Technology Innovation (Beijing) Co., Ltd, Beijjing, China

[3] WEL Research Institute, 1300 Wavre, Belgique

[4] Laboratoire Roberval, UTC, Sorbonne Universités, Université de Technologie de Compiègne, Centre de recherche Royallieu, CS60319, 60203 Compiègne Cedex, France

[5] Curtin Corrosion Centre, WA School of Mines: Minerals, Energy and Chemical Engineering, Faculty of Science and Engineering, Curtin University, Perth, WA, Australia

*Corresponding author: jishuai.li@outlook.com

Supplementary Material

Fig.S1 shows the maximum width (measured with a Vernier calliper) and overall thickness of the deposition along the rod advancing direction for two processing conditions for a four-layer deposition. These two conditions have been selected to establish the effect of the advancing speed on the deposition geometry. A stationary region, i.e., the zone where the conditions are constant during deposition, is particularly interesting to study. A lower *v* increases the deposition width in that stationary region (Fig.S1a). This is due to a substantial amount of material pushed aside at the bottom of the consumable rod forming a bulge. Fig.S1b compares the same deposition conditions and shows that operating with lower *v* leads to thicker layers.

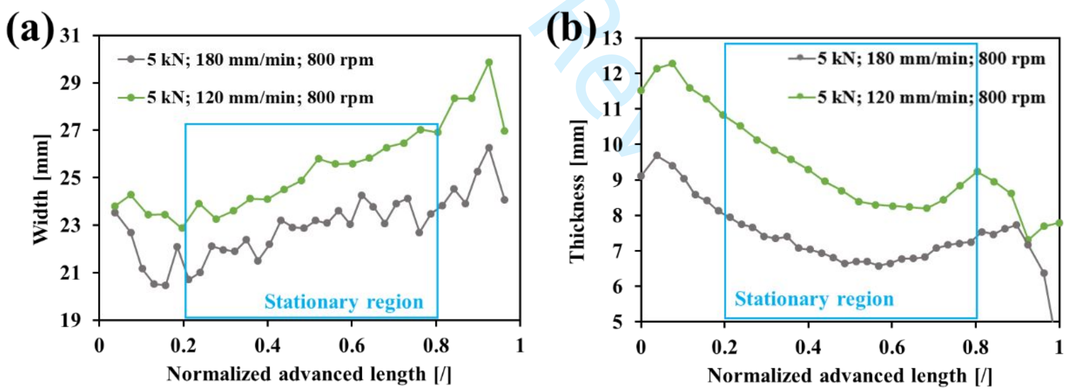

Fig. S1. Effect of the advancing speed of deposition on the maximum width (a) and overall thickness (b) of a four-layer deposition. These measurements are performed along the normalized advanced length, i.e., the current measurement position divided by the total length of the deposition.